Composites Science and Technology 254 (2024) 110695

Contents lists available at ScienceDirect

Composites Science and Technology

journal homepage: www.elsevier.com/locate/compscitech

Cycle-consistent generative adversarial networks for damage evolution analysis in fiber-reinforced polymers based on synthetic damage states

Ramon Helwing *, Selim Mrzljak, Daniel Hülsbusch, Frank Walther

Chair of Materials Test Engineering (WPT), TU Dortmund University, Dortmund, Germany

ARTICLE INFO

Keywords:
Defects
Fatigue
Damage mechanics
X-ray computed tomography
Deep learning

ABSTRACT

Analyzing computed tomography (CT) scans is challenging and time-consuming due to their high complexity. Machine learning, particularly in the form of segmentation techniques, has emerged as the state-of-the-art approach for defect detection in parts and materials. However, the lack of pixel-accurate labeled training data remains a significant challenge. This paper presents a damage state transformation approach based on a cycle-consistent generative adversarial network (CycleGAN) using fatigue damage states of fiber-reinforced polymers. The generated synthetic data is visually almost indistinguishable from real data. Introduced damage can be determined by calculating the damage removed during the transformation from a high-damage state to a low-damage state. Using multiple transformation steps in detecting and distinguishing different damage states the effectiveness is demonstrated. In addition, the virtual addition of damage to undamaged specimens is investigated. The results show that certain damages exhibit chaotic generation across successive slices while maintaining semantic connections in specific regions across multiple slices. Overall, this research presents a valuable approach for improved self-supervised damage detection and characterization in CT scans, with potential applications in materials analysis and structural health monitoring.

1. Introduction

Computed Tomography (CT) is a powerful technique, especially for the detection of damage in fiber-reinforced polymers. Identifying defects, and visualizing the material helps to understand interactions in the material. However, CT datasets contain a large number of cross-sectional images taken from different slices of the body. Each of these images contains millions of pixels or voxels (3D pixels), leading to an enormous total number of data points. Analyzing this high volume of data requires a lot of computing power and time. Qualitative expert analysis based on comparing different scans is time-consuming and challenging to verify due to the massive amount of data. Therefore, segmentation methods are used to quantify the damage, but the results remain difficult to obtain and interpret.

Machine learning is increasingly used in favor of traditional segmentation methods based on image processing with thresholding and further improves segmentation quality [1–4]. State-of-the-art segmentation models are based on deep learning, which recognizes highly complex semantic relationships from the data and thus leads to accurate and robust segmentation results, especially for difficult applications of medial CT or satellite image analysis [5–7]. While open-source training data sets are available for many segmentation applications, they are nonexistent for highly specialized tasks. Therefore, different approaches are taken to compensate for this need with regard to the analysis of damage in fiber-reinforced polymers.

Some machine learning algorithms can achieve stable predictions with smaller data sets, while deep neural networks may exhibit overfitting. This makes an algorithm like random forest an appropriate choice for limited training data [8]. Deep neural networks offer unique advantages in certain scenarios because they can learn complex representations and capture intricate patterns in the data. This makes them highly effective for tasks such as image segmentation despite the risk of overfitting, especially for small and variable datasets. Labeling for segmentation is time-consuming because it requires manual annotation of each pixel or region in an image, requiring a high level of attention to detail and accuracy. As a result, generating labeled data becomes a time-consuming task, further impacted by the potential introduction of human bias, particularly during pixel-level annotation for segmentation [2]. These noisy labels affect the performance of the network, especially for small data sets or when the labels have a general bias [9,10].

* Corresponding author.
E-mail address: ramon.helwing@tu-dortmund.de (R. Helwing).

https://doi.org/10.1016/j.compscitech.2024.110695
Received 31 July 2023; Received in revised form 12 February 2024; Accepted 2 June 2024
Available online 3 June 2024

To take advantage of recent advances in deep learning for the analysis of fiber-reinforced materials, various strategies are employed. E.g., priory performed foreground segmentation reduces the variance of the background data [11]. This approach simplifies segmentation by dividing the segmentation into subtasks, reducing the demands on the machine learning algorithm's flexibility and decreasing the required training data. Moreover, transfer learning proves valuable by using large, freely available data sets to acquire an appropriate pre-trained network. The network for defect detection is obtained by fine-tuning through the acquired dataset [12–14]. Another widely used strategy is data augmentation, which involves generating additional data through operations such as random crop, flipping, resizing, or rotating. By expanding the training data set in this way, the model can learn a larger range of patterns and improve its performance [15–17]. Additional physical data augmentation like random rotation and adapted acquiring settings lead to a variational data set of this same specimen [18]. Advanced deep learning methods like synthetic image generation based on conditional generative adversarial networks (cGANs) and variational autoencoders are used to increase the amount of training data [19]. Cheng et al. trained the segmentation network not directly on the labeled data, but the discriminator approach evaluates the generated data [20]. This GAN approach shows a good generalization of the segmentation network for the experimental data.

By reducing the complexity of the segmentation task in the training data a semi-automatic generation of training data can be applied. High-resolution methods for volume analysis (e.g., CT) are used for capturing detailed and precise information about the objects or regions to be segmented. This data is then used as a reference to train and validate models for the segmentation of low-resolution methods (e.g. data from ultrasonic scans). By using this high-quality data for labeling, the models can learn to better capture fine details and subtle differences in input information and produce accurate segmentation results. This enhances the accuracy and quality of the segmentation and automates the generation of training data [21]. In some cases, however, the correct overlay is difficult to achieve. Badran et al. found that tilting microscopy images relative to the reference CT images resulted in the misalignment of the two images. Therefore, it may be necessary to take steps to achieve the correct superposition [18]. By selectively integrating stitched fibers into a specimen generated specifically for training, segmentation can be performed based on the presumed static position of the fibers. The generated segmented data is then used to detect fibers that are in random orientation [22].

Simulation-based generated material responses enrich the training data and can partially completely avoid training with real-world experimental data using the simulative introduced defects is based on the influenced of the lambda wave propagation, strain field and thermal conduction, creating training data from the defect position and size and the material response [13,20,23]. The segmentation model is validated against experimentally recorded data and demonstrates high generalization despite being trained on simulated data [24,25]. However, generating visually similar analog data in computed tomography is challenging and requires expertise [26].

Especially for CT scans, labels are only provided at the image or scan level. Supervised learning is then applied to categorize different image categories based on these labels. By analyzing the network's activity, the discriminative regions in the image and the location of the object specific to the target class can be identified. High discriminatory regions, estimated by class activation map (CAM), give the segmentation mask. The mask is either processed for segmentation or used as pre-segmentation for further training [27,28]. Due to the implementation of the network, their segmentation is only available with a low resolution. Further refinement of the segmentation result is achieved by using post-processing. However, heat maps of different CAM methods differ greatly from each other, even when the same classification model is used. Therefore, the usefulness of CAM methods for segmentation can be questioned [29].

Neural networks are utilized for regenerating a statistical target distribution by generating visually indistinguishable images from the target data through the implementation of a generative adversarial network (GAN). The generator network of the GAN aims to produce data that closely resembles the target distribution, while the discriminator network of the GAN distinguishes real data from the generated data. Through iterative training, both networks adapt and enhance their capabilities continuously. However, unlike traditional GANs that generate images from random noise, input images are used as input for the generator. By different training methods, this autoencoder-like generator can act like an image transformation, which repairs or introduces damage in the input image [30]. The segmentation can be carried out by comparing the initial image with defect-free output images [31].

Other authors use CycleGANs for this transformation. CycleGANs, in contrast to conventional GANs that generate images from random noise, are composed of two generator networks and two discriminator networks. The first generator network converts the input data to a target domain, while the second generator network converts the target domain data back to the original input domain. The two discriminator networks assess the quality of the generated data from both directions. The cyclic structure of the network allows it to learn the mapping between two domains and generate realistic images or data with the desired characteristics [32]. The presented method achieves superior results to defect localization by CAM and comparable segmentation performance to the supervised state-of-the-art segmentation methods. It also recognizes anomalies that are not present in the training data [33,34]. However, the usability under artifact formation and noise of real CT datasets still needs to be verified.

In this paper, a methodology of the virtual transformation of the damage states of fatigued specimens into lower or higher damage states is developed. The phenomenological appearance of the damage is detected and recreated by a CycleGAN. The method is applied to and demonstrated for the damage evolution of glass fiber reinforced polymer in the high cycle fatigue (HCF) and very high cycle fatigue (VHCF) regime. Be recreating a lower damage state, e.g. the initial damage state, the damage in the specimen is separated by a self-supervised segmentation based on labeling on the CT scan level. Since the segmentation is based on the data itself and not on the segmentation labels, this method does not require the time-consuming and user-influenced pixel-by-pixel labeling that is necessary with supervised segmentation.

2. Material and experimental methods

2.1. Material

In this research, the CycleGAN approach is applied to the damage evolution in glass fiber-reinforced epoxy resin for synthetic recreation and validation of its applicability. The laminate structure comprises a quasi-isotropic 8-harness satin weave with 16 fabric layers and a fiber volume fraction of 45 %. The fiber material used is Hex-Force 07781 1270 (Hexcel) with a fiber diameter of 9 μm and Silane TF970 sizing, and the matrix system employed is HexPly 914 (Hexcel). To ensure minimal resin voids, the specimens undergo a curing process using an autoclave [35].

2.2. Fatigue testing

Fatigue tests are conducted at room temperature using load control. With regard to the high-cycle fatigue (HCF) regime, the tests considered for this investigation are performed at a testing frequency of 6.8 Hz using a servo-hydraulic testing system (Shimadzu EHF-UV100, maximum force $F_{max} = \pm 100$ kN, equipped with 30 kN load cell). For the very high-cycle fatigue (VHCF) regime, a resonance fatigue testing system (Rumul Gigaforte 50, $F_{max} = \pm 50$ kN, maximum force amplitude $F_a = \pm 25$ kN) is utilized, capable of reaching a testing frequency of approximately 1000 Hz. In both systems, a constant sinusoidal tension-

tension load is applied with a load ratio (R) of 0.1, indicating cyclic loading in the tensile range where the minimum stress is 10 % of the maximum stress. The investigated maximum stress within the HCF regime is set at 173 MPa, while for the VHCF regime, it is 95 MPa [35]. Due to self-heating, the specimen is actively cooled, leading to changes in core temperature of maximum 15 K. On the surface of the specimen no significant change in temperature can be measured [36].

For both regimes, specimens are cycled up to approximately 0.3 %, 20 %, and 80 % of their fatigue life and then removed from the testing system, and subsequently, the damage is analyzed using computed tomography. The fatigue life is defined by the mean value of numbers of cycles until specimen failure for all specimens investigated under the same loading and testing conditions (results are published in Ref. [35]). A special specimen geometry (Fig. 1) is chosen for both testing machines to meets the requirements of the computed tomography in chapter 2.3.

2.3. CT scanning

After fatigue loading, the specimens are examined by X-ray micro-computed tomography (μCT) using a Nikon XT H 160 system with a focus spot size of 3 μm. The rotation axis of the specimen is positioned at a distance of 54.6 mm from the source, which results in a geometric magnification of 18.14 due to the detector-source distance of 990.8 mm. Detector with a resolution of 1008 × 1008 pixels, which enables a voxel size of 7 × 7 × 7 μm^3 in this scan configuration To facilitate in-situ scanning during load application, an in-situ CT stage (Deben UK CT5000) is utilized with a tubular load frame made of low X-ray attenuating vitreous glassy carbon (Fig. 2). With the usage of a contrast agent, the ability to detect damage is enhanced. The contrast agent consists of 18 g zinc iodide, 3 ml distilled water, 3 ml isopropyl alcohol and 3 ml Kodak Photo-Flo wetting agent. Cracks are penetrated by the contrast agent due to the capillary effect, which increases the X-ray absorption, thereby improving the detectability of damage significantly [37,38]. In addition, the application of a tensile load further enhances the visibility of defects by reducing the effects of crack closure. The static loading is set to 90 % of the maximum stress applied during fatigue loading, to ensure a valid representation of the damage stage. In this study the following CT acquisition parameters were used: tube voltage 120 kV, tube current 59 μA, exposure time 354 ms, 1583 projections, 8-fold superimposition of each image. The CT scans are performed sequentially so that each cycled specimen is scanned only once since the contrast agent and the superposed loads during the CT scans alter the

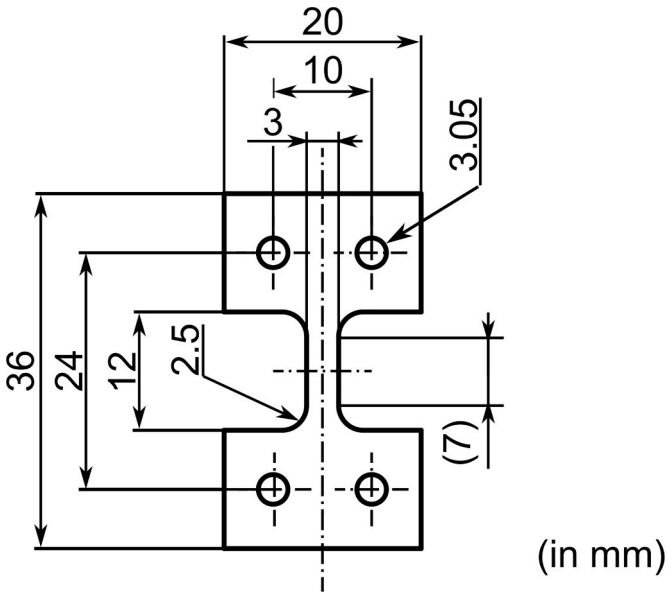

Fig. 1. Specimen geometry for μCT (in mm).

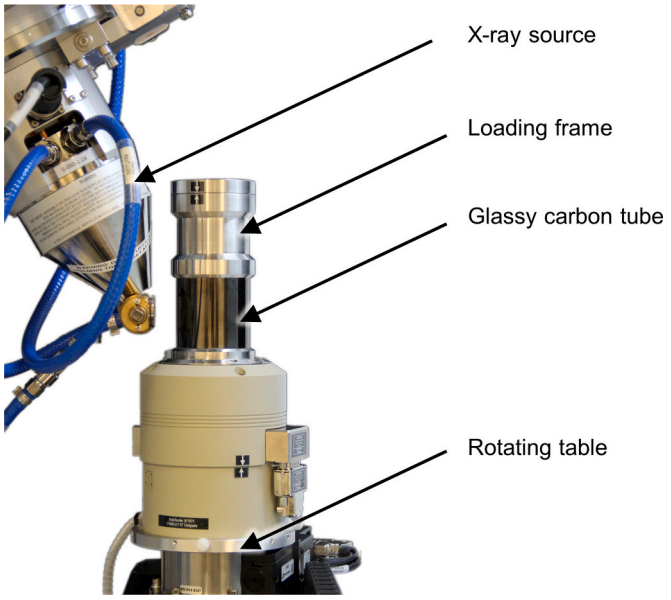

Fig. 2. In-situ CT loading frame with X-ray source.

damage evolution of fiber-reinforced polymers. Different CT scans of different damage states for the HCF regime are shown in (Fig. 3). This makes it impossible to directly observe and compare the damage evolution in only one specimen without the influence of the static load and contrast agent [39]. The reconstruction takes place by filtered back projection utilizing the software CT Pro (Nikon). To reduce the potential influence of degrading filament on the CT scan gray levels, the reconstructed CT scans are normalized by the gray level of the matrix and fiber.

2.4. Deep learning method

The framework of the CycleGAN consists of two generators (G_{AB} and G_{BA}) and discriminators (D_A and D_B). The data flow and the application of the loss functions in the CycleGAN are shown in Fig. 4. The generator G_{AB} maps an image from dataset A to a representation of dataset $\overline{B}$ by mimicking the characteristic features of dataset B. The synthetic dataset gets evaluated by the discriminator D_B, which is trying to predict if the input is from B or $\overline{B}$. The same structure exists to map dataset A to $\overline{A}$. To avoid a random permutation of the transformation and therefore diverging from the original image, the synthetic dataset is retransformed back by the other generator. The resulting $\overline{A}$ and $\overline{B}$ are compared to their instances of the original datasets A and B. These cycle consistency losses are to prevent inconsistent transformation.

As network architecture for the generator a residual UNet is used [40]. The architecture follows a U-shaped structure with an encoder for information extraction and a decoder for information recovery. The special feature is the so-called residual learning, in which the network learns the difference between expected and predicted results to facilitate training. The combination of UNet and residual learning allows the network to utilize deep structures for complex pattern recognition while improving trainability. The skip connection enables a direct flow of information between the encoder and decoder blocks and thus improves the performance of a generator [41]. A detailed overview of the generator structure is giving in Fig. 5. Analogs of Zhu et al. two 70 × 70 PatchGANs are used as discriminator [32,42]. The discriminators network follows the structure in Ref. [43]. As a deep learning framework, PyTorch is utilized. The training is carried out with an Nvidia RTX A5000 GPU and an Intel Xeon Silver 4210R CPU.

In CycleGAN, the generators are trained using a composite loss function. The generator loss, denoted as L_{gen}, is calculated based on the

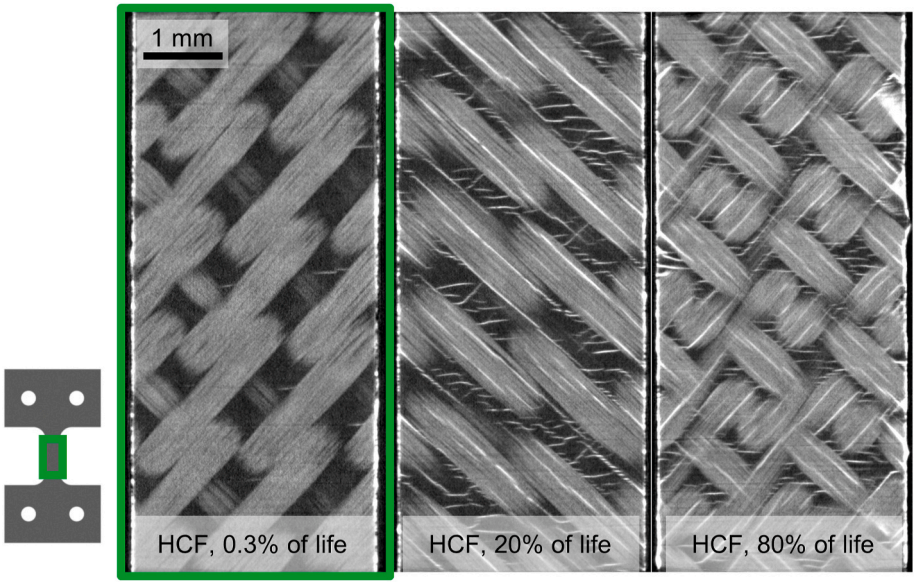

Fig. 3. CT scan of the fatigued fiber-reinforced polymers with different damage states.

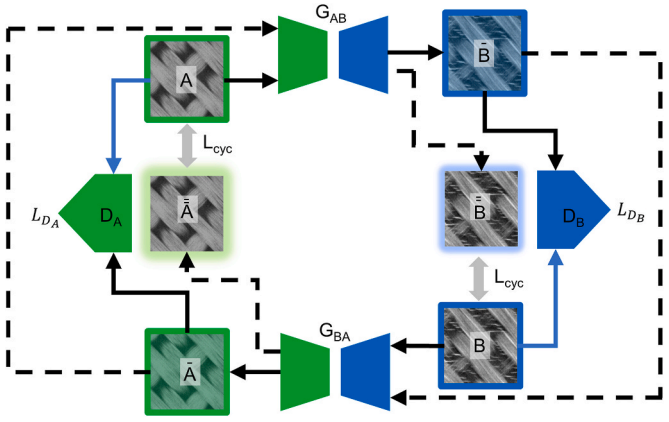

Fig. 4. The framework of a Cycle-consistent generative adversarial network (CycleGAN).

L1 loss between the output of both discriminators D_B and D_A and the synthetic data generated by the contradiction generators G_{AB} and G_{BA}. This loss is computed for a batch size of N and is defined as:

$$L_{gen} = \frac{1}{N}\sum_{i=0}^{N}\left|D_B(G_{AB}(A_i)) - 1\right| + \frac{1}{N}\sum_{j=0}^{N}\left|D_A(G_{BA}(B_j)) - 1\right|$$

The cycle consistency loss, denoted as L_{cyc}, measures the L1 distance between the reconstructed data and the original data. It is calculated by back-transforming the data using the generators G_{AB} and G_{BA} and comparing it to the input data. The loss is given by:

$$L_{cyc} = \frac{1}{N}\sum_{i=0}^{N}\left|A_i - G_{BA}(G_{AB}(A_i))\right| + \frac{1}{N}\sum_{j=0}^{N}\left|B_j - G_{AB}(G_{BA}(B_j))\right|$$

To improve the performance for periodic patterns an identity mapping loss is introduced [33]. This loss control measures the discrepancy of the transformation form $G_{BA}(A) = A$ and $G_{AB}(B) = B$.

$$L_{id} = \frac{1}{N}\sum_{i=0}^{N}\left|A_i - G_{BA}(A_i)\right| + \frac{1}{N}\sum_{j=0}^{N}\left|B_j - G_{AB}(B_j)\right|$$

To control the relative importance of the composed loss function L_{gen}, the cycle consistency loss (L_{cyc}), and the identity mapping loss (L_{id}), scaling factors λ_{cyc} and λ_{id} are introduced. The overall generator loss (L_{Gen}) is then calculated as:

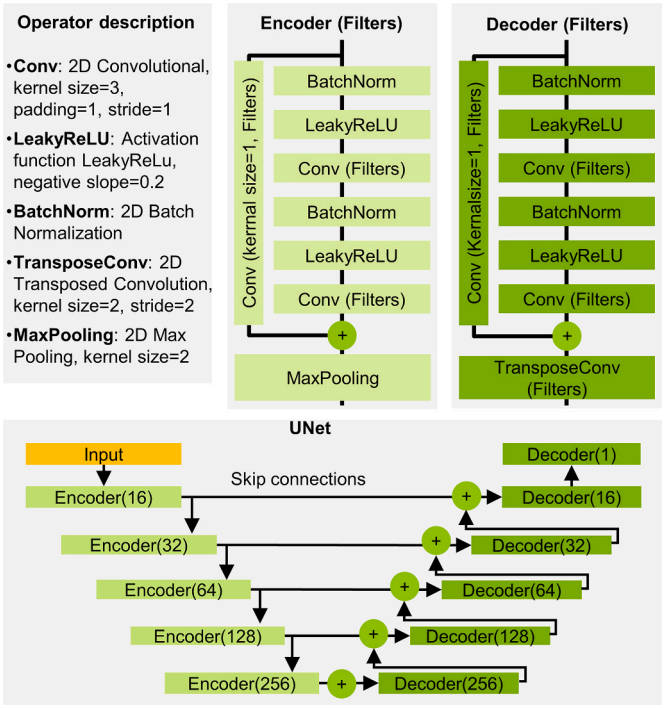

Fig. 5. Structure of the UNet used as generator of the CycleGAN.

$$L_{Gen} = L_{gen} + \lambda_{cyc}L_{cyc} + \lambda_{id}L_{id}$$

During training, λ_{cyc} is set to 10 and λ_{id} is set to 5.

The discriminator loss uses the mean squared error as the loss function. The discriminator losses for D_A and D_B, denoted as L_{D_A} and L_{D_B} respectively, are calculated as:

$$L_{D_A} = \frac{1}{2N}\sum_{i=0}^{N}\left(\left|D_A(A_i) - 1\right|^2 + \left|D_A(G_{BA}(B_i))\right|^2\right)$$

$$L_{D_B} = \frac{1}{2N}\sum_{j=0}^{N}\left(\left|D_B(B_j) - 1\right|^2 + \left|D_B(G_{AB}(A_j))\right|^2\right)$$

The training process utilizes the Adam optimizer with a learning rate

of 0.002. After 200 epochs, the learning rate is linearly decreased until it reaches 0 at epoch 300. To balance training efficiency and hardware requirements, a batch size of 8 is chosen, and the training is performed on randomly selected 256 × 256 image patches. Data augmentation is applied by randomly flipping the patches horizontally and vertically. The training of the CycleGAN model takes approximately 6 h. After training, the generator is used to transform data from one CT scan of a damage state into a synthetic version of a high or low-damage state (Fig. 6). Instead of patches, a full-sized image is processed. Due to the flexibility of PyTorch, no adaption of the network architecture or patching is necessary.

By training CycleGAN with different data sets, a transformation of a high damage state data set into different synthetic data sets with lower damage states is achieved. Due to the differences in the damage mechanisms, the texture of the fiber and matrix gets removed and the damage present gets highlighted for better evaluation. The detection of the image is carried out by subtracting the high damage state input data and the transformed output of generator G_{AB}, the difference between both characteristics is calculated. To highlight new accumulated damage between two damage states, a dataset of a high damage state is transformed into different lower synthetic damage states. The training of the CycleGAN is carried out with the introduced training scheme with the different damage state datasets, generated for the initial undamaged specimen state (0 %) and after cycling until 0.3 %, 20 %, and 80 % of their fatigue live. The different generators are used to transform a high damage state image to a lower damage state image. The difference between the input image and the transformed image of each generator represents the introduced damage between these two damage states. The pixel-by-pixel subtraction of CT scans of a higher damage state from the synthetically generated lower damage state leads to the detection of the introduced damage between the two states (Fig. 7). For damage visualization, the difference is multiplied by 1.5 and assigned color channels (red, green, blue). To avoid mixing different colors, only the largest difference in a pixel value is considered. It is emphasized that the labels on pixel levels did not have to be experts to create the training data. The model, therefore, generated this expert knowledge from the training data itself.

3. Results

3.1. Artifacts and image quality

To demonstrate the transformation capability of the generator models, the initial specimen condition is selected as dataset A, while the CT scan with the highest damage state (80 % fatigue life, HCF) is selected as dataset B. The evaluation of the transformation quality in terms of an artifact-free and geometrically correct mapping between the

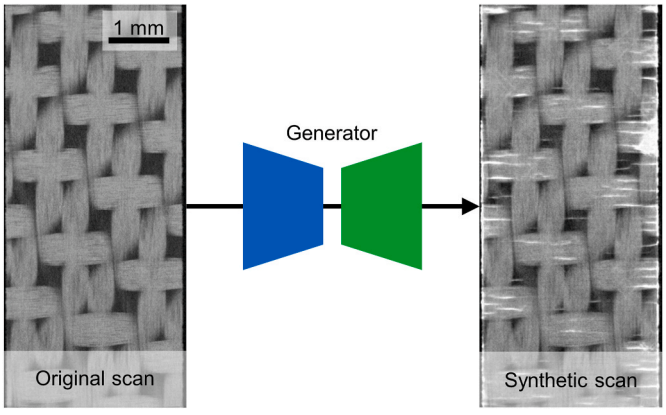

Fig. 6. Transformation with the generator of a slice of a CT scan into a higher damage state.

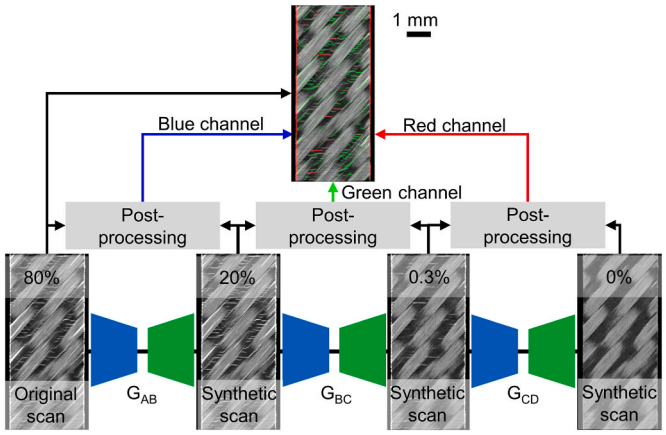

Fig. 7. Framework for automatic highlighting of the damage corresponding to the damage states.

original scan and the synthetic data is performed by visual inspection in Fig. 8. Attention is paid to the preservation of local details. The removal of defects (transformation for high to low damage state) is separately evaluated for introducing synthetic defects (transformation from low to high damage state, Fig. 9).

The artifacts that occur can only be distinguished in the detailed view. Differences like small deviations in the transformation of low-intensity fiber content remain in the synthetic dataset. Low-intensity fiber content is removed to a minor extent so that the matrix content increases slightly (Fig. 8 a, b). However, small details like fiber texture elements remain in the transformed CT slices. Matrix cracks, resulting mostly from adjacent interfiber failure, are completely removed in the matrix-rich region, leading to an artifact-free transformation of this damage mechanism (Fig. 8 a, b). Datasets of removed defects can be detected due to the lack of texture generation in defects such as delamination (Fig. 8 c) and oversharpening on some fiber of the scan (Fig. 8 d). However, the artifacts are barely visible, even in the detailed view.

When damage is introduced synthetically (Fig. 9), only barely perceptible artifacts such as slightly blurred edges of some fiber-matrix interface (Fig. 9 a, b) and large-area defects such as delaminations (Fig. 9 c) are generated. A similar effect occurs for some interfiber failures (Fig. 9 d).

The results from the user observations can confirm the overall high precision of the transformation both in the synthetic error generation and in the generation of the initial state in terms of authenticity and visual quality.

3.2. Model-based synthetic damage introduction

Synthetic damage is generated using information from just a single slice, with no exchange between slices. By comparing the synthetically introduced defects between successive slices, it is possible to determine how consistently damage from different damage mechanisms can be transferred (Fig. 10). The appearance of matrix cracks in the matrix-rich areas differs between adjacent slices leading to the development of distinct phenological characteristics (Fig. 10 a). On the other hand, other damage mechanisms, such as interfiber failure, tend to show stability across different slices (Fig. 10, b). Delamination also predominantly appears in adjacent slices at the same location, demonstrating a plausible evolution of damage (Fig. 10, c). However, the spacing between matrix cracks remains consistent across different data planes. In particular, delamination tends to occur at comparable locations in successive slices.

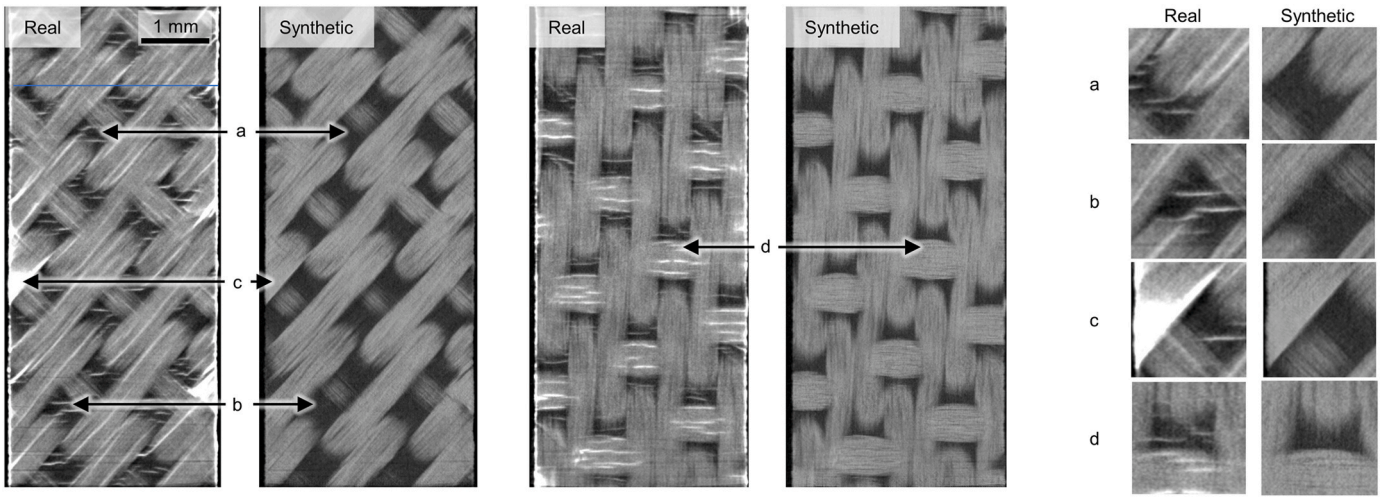

Fig. 8. Comparison of CT slices of high damage state with synthetic damage-free initial damage state (removal of defects).

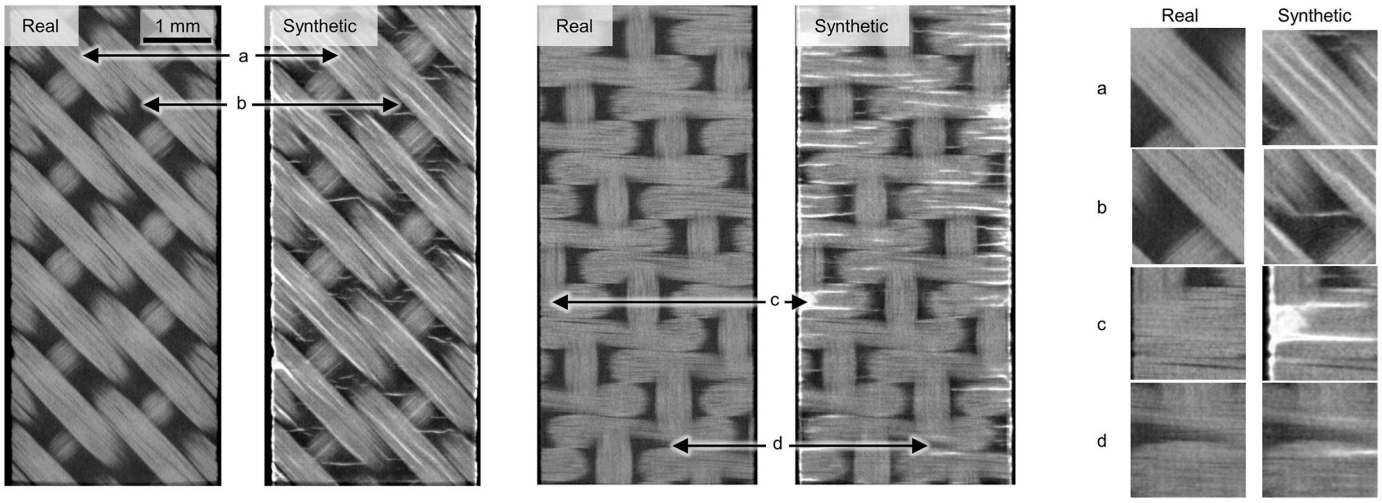

Fig. 9. Comparison of CT slices from initial damage state with synthetic introduced high damage state (damage introduction).

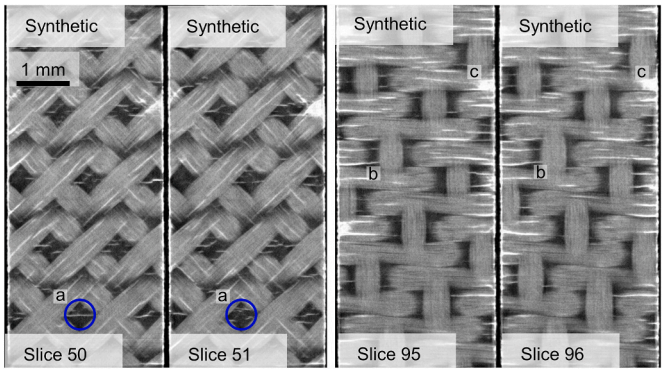

Fig. 10. Synthetically generated damage between adjacent slices.

3.3. Separation of damage based on the damage stage

Training the described CyclicGAN with different data sets enables the transformation of a damage state data set into different synthetic data sets with lower damage states. The detection of the image is carried out by subtracting the high damage state input data from the transformed low damage state output of generator G_{AB}. Due to the difference in the damage state, the texture of the fiber and matrix gets removed and the damage gets highlighted.

For the HCF regime (Fig. 11), the damage evolution based on the CycleGAN is introduced with transversal cracks between the initial state and 0.3 % of the expected fatigue life (Fig. 11). The fatigue damage mainly occurs in the form of interfiber failure, which further expand into matrix cracks. Especially the edge effect of the laminate can be noticed. While matrix cracks start predominantly on the edge, interfiber failures often start in the middle of the laminate a grow to the laminate edges. The adhering contrast agent on the surface of the specimen gets clearly and correctly recognized, which is due to the avoided usage of contrast agents for the initial damage stage. New cracks in the matrix and fibers show, that the crack density increased with cyclic loading. Interfiber failures in a 45-degree direction are predominately introduced between 0.3 % and 20 % of the fatigue life. Delamination is only introduced in the late stage of fatigue, between 20 % and 80 %.

In the VHCF regime, almost no damage is introduced up to 0.3 % of the expected fatigue life (Fig. 12). Only a small amount of transversal matrix cracks is detected by the algorithm. Worth noting is the additional transversal matrix cracks, which get introduced between 20 % and 80 % of the fatigue life. Also, small cracks between fiber bundles and the matrix material are highlighted. Due to insufficient transformation, artifacts like blue areas occur in the analyzed VHCF data. In some

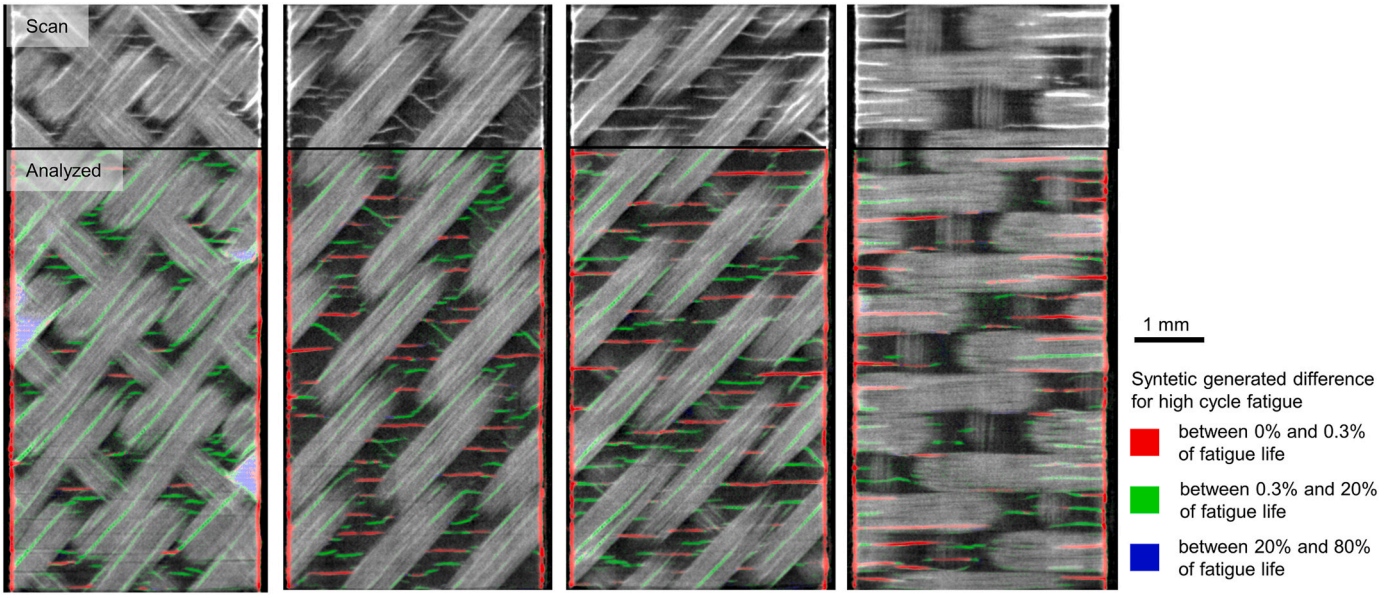

Fig. 11. Synthetically generated differences between damage states of high cyclic fatigue.

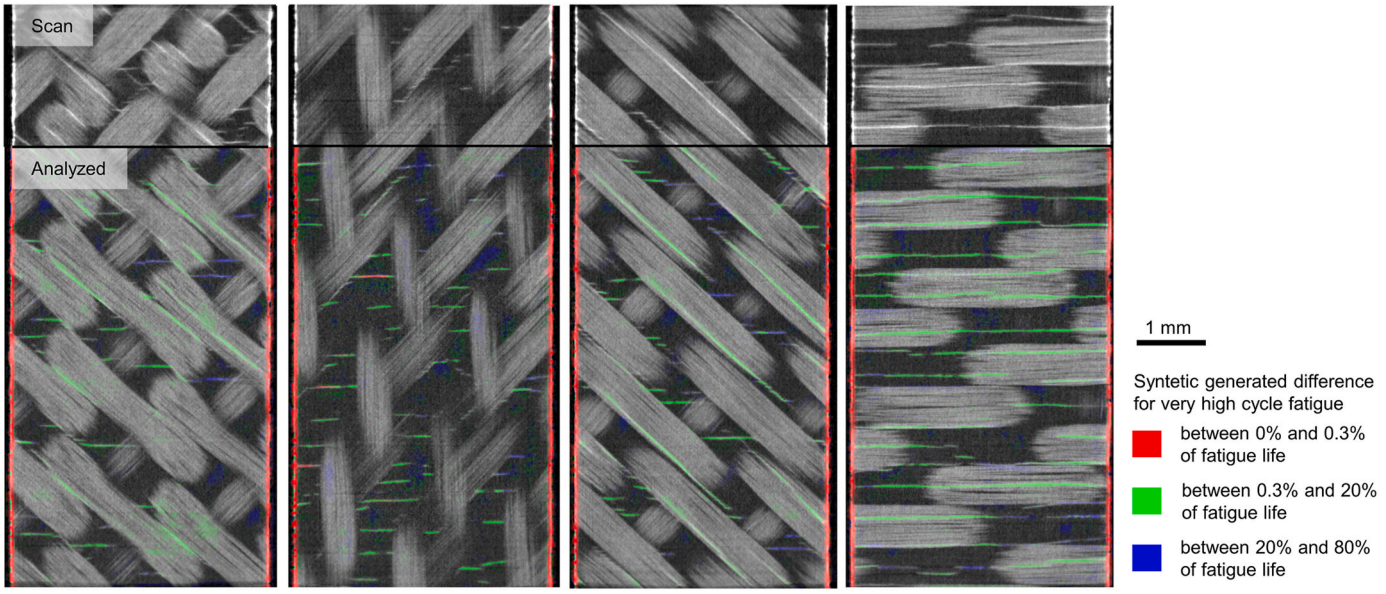

Fig. 12. Synthetically generated differences between damage states of very high cyclic fatigue.

regions, a green scattering in regions of fibers also shows the algorithm's difficulties in precisely matching the gray scaling.

Due to the constant acquisition parameters between the CT scans, it is expected that deviations between the data will be reflected in a change of the damage state and not in artifacts in the CT acquisition or the reconstruction.

The occurring artifacts of the defect detection can be traced back to cumulative errors of the different transformations. A pronounced over-sharpening effect can be found in the images by comparing the input data and the three-times transformed image. In addition, not all damages in the image are removed completely. Some artifact defects are still in the image. Especially, delamination failed to be removed completely, introducing insufficient damage detection. However, in general, multiple transformations of a dataset into different virtual damage stages are possible with this framework.

4. Discussion

The transformation between damage states offers the possibility to differentiate between different damage mechanisms, including differentiation according to the time of occurrence in the fatigue life. However, the training of these models is relatively expensive. The use of different sub-networks requires an increased training effort, which is higher compared to supervised segmentation. Nevertheless, these self-supervised approaches offer the advantage of reduced human workload since the process is largely automated. However, the focus here is primarily on optical plausibility. The resulting physical effects are only probabilistically represented by the CycleGAN. This is especially true for defect generation, which produces different damage in adjacent sections. Nevertheless, certain defect phenomena also occur in adjacent slices during defect generation. This could indicate the recognition of characteristic regularities present in the datasets, resulting in high stability of the synthetic damage generation. However, a generator of a

CycleGAN can encode output information in the form of high-frequency signals. The detection or recreation of local, random patterns by CycleGAN cannot be ruled out at this time [44]. The multiple transformations lead to an increased number of artifacts and prevent the complete removal of the defects. Particular training with datasets with small differences seems less successful and more subjected to less accurate transformation and artifacts. However, within the experiments the search for the optimal hyperparameters and model parameters was not in focus, so that the possible improvement potential is not fully exploited. The transformation between damage states offers the possibility to differentiate between different damage mechanisms, including differentiation according to the time of occurrence in the fatigue life.

5. Conclusions and outlook

In conclusion, this paper presents a novel, self-supervised approach for detecting defects in e.g., CT images, specifically focusing on fiber-reinforced polymers. The developed method involves the synthetic generation and removal of defects, resulting in high-quality model outputs that in general cannot be distinguished from real data by experts. Despite independently generating defects in adjacent layers, some local damage remains semantically connected between the layers, while others do not exhibit a coherent pattern. This observation could suggest either a chaotic development of damage or mechanisms that are not evident in the visible boundary conditions captured by CT scans. Furthermore, the detection of defects through the transformation from a highly damaged state to a less damaged state allows for the detection of introduced damage solely based on experimental boundary conditions, utilizing self-supervision. The absence of pixel-level labels eliminates the need for labor-intensive training data creation. Moreover, applying multiple transformations to represent different damage states makes it possible to detect and visualize fatigue life-related damage mechanisms. The proposed approach enables the preparation of data for an intuitively understandable representation of the evolution and interaction of damage within the material. Overall, this research contributes valuable insights into defect detection, synthetic generation, and the analysis of damage mechanisms in fiber-reinforced polymers using deep learning methods. The developed methodology offers promising opportunities for further advancements in the field and opens up possibilities for improved understanding and characterization of material damage.

CRediT authorship contribution statement

Ramon Helwing: Conceptualization, Data curation, Formal analysis, Methodology, Software, Validation, Visualization, Writing – original draft. **Selim Mrzljak:** Investigation, Methodology, Writing – review & editing. **Daniel Hülsbusch:** Investigation, Writing – review & editing. **Frank Walther:** Project administration, Resources, Supervision, Writing – review & editing.

Declaration of generative AI and AI-assisted technologies in the writing process

During the preparation of this work, the authors used ChatGPT to improve the readability of the manuscript. After using this tool/service, the authors reviewed and edited the content as needed and take full responsibility for the content of the publication.

Declaration of competing interest

The authors declare that they have no known competing financial interests or personal relationships that could have appeared to influence the work reported in this paper.

Data availability

Data will be made available on request.

Acknowledgments

The authors thank Fachagentur Nachwachsende Rohstoffe e.V. (Agency for Renewable Resources) for their financial support (project no. 2220NR090D).

The authors further thank the German Research Foundation (Deutsche Forschungsgemeinschaft, DFG) and the Ministry of Culture and Science of North Rhine-Westphalia (Ministerium für Kultur und Wissenschaft des Landes Nordrhein-Westfalen, MKW NRW) for their financial support within the Major Research Instrumentation Program for the high-frequency fatigue testing system Rumul Gigaforte 50 (project no. 424760282) and the high-performance workstation of the dual tube computed tomography system (project no. 459685720).

References

[1] W. Cao, Y. Wu, B. Sun, B. Gu, M. Hu, Impact crack quantification analyses in 3-D angle-interlock woven composite using image segmentation method, Eng. Fract. Mech. 269 (2022), https://doi.org/10.1016/j.engfracmech.2022.108529.
[2] V. Pidou-Brion, Y. Le Guilloux, Active yarn meshes for segmentation on X-ray computed tomography of textile composite materials at the mesoscopic scale, Compos. Struct. 281 (2022), https://doi.org/10.1016/j.compstruct.2021.115084.
[3] S. Mrzljak, B. Zanghellini, L. Gerdes, R. Helwing, R. Schuller, G. Sinn, et al., Effect of carbon nanofibre orientation on fatigue properties of carbon fibre-reinforced polymers, J. Compos. Mater. (6) (2023) 57, https://doi.org/10.1177/00219983221150496.
[4] C.W. Foster, L.N. Collins, F. Panerai, S.A. Roberts, Assessing thermophysical properties of parameterized woven composite models using image-based simulations, Compos. Sci. Technol. 241 (2023), https://doi.org/10.1016/j.compscitech.2023.110136.
[5] R. Hossain, R.B. Ibrahim, H.B. Hashim, Automated brain tumor detection using machine learning: a bibliometric review, World Neurosurg. 175 (2023), https://doi.org/10.1016/j.wneu.2023.03.115.
[6] G. Jain, D.P. Singh, J. Choudhary, Flynet–Neural network model for automatic building detection from satellite images, J. Indian Soc. Remote Sens. (2023), https://doi.org/10.1007/s12524-023-01703-2.
[7] Y. Xu, X. Xue, Z. Sun, W. Gu, L. Cui, Y. Jin, et al., Deriving agricultural field boundaries for crop management from satellite images using semantic feature pyramid network, Rem. Sens. (11) (2023) 15, https://doi.org/10.3390/rs15112937.
[8] R.S. Da Vianna, A.M. Pereira, R. Leiderman, J.D. Vieira, Characterization of pultruded glass-fiber reinforced polymers with two-step homogenization, Mater. Res. 26 (2023), https://doi.org/10.1590/1980-5373-mr-2022-0252.
[9] J. Gutter, J. Niebling, X.X. Zhu, Analysing the interactions between training dataset size, label noise and model performance in remote sensing data, in: IEEE International Geoscience and Remote Sensing Symposium, Kuala Lumpur, Malaysia, 2022, https://doi.org/10.1109/igarss46834.2022.9884570.
[10] E. Vorontsov, S. Kadoury, Label noise in segmentation networks: mitigation must deal with bias, in: S. Engelhardt, I. Oksuz, D. Zhu, Y. Yuan, A. Mukhopadhyay, N. Heller, et al. (Eds.), Deep Generative Models, and Data Augmentation, Labelling, and Imperfections, Springer International Publishing, 2021, https://doi.org/10.1007/978-3-030-88210-5_25.
[11] S. Sheiati, X. Chen, Deep learning-based fatigue damage segmentation of wind turbine blades under complex dynamic thermal backgrounds, Struct. Health Monit. (2023), https://doi.org/10.1177/14759217231174377.
[12] K. Deng, H. Liu, L. Yang, S. Addepalli, Y. Zhao, Classification of barely visible impact damage in composite laminates using deep learning and pulsed thermographic inspection, Neural Comput. Appl. (15) (2023) 35, https://doi.org/10.1007/s00521-023-08293-7.
[13] Y. Wang, Q. Luo, H. Xie, Q. Li, G. Sun, Digital image correlation (DIC) based damage detection for CFRP laminates by using machine learning based image semantic segmentation, Int. J. Mech. Sci. 230 (2022), https://doi.org/10.1016/j.ijmecsci.2022.107529.
[14] L. Gerdes, S. Berger, J. Saelzer, P. Franck, R. Helwing, A. Zabel, et al., Application-oriented digital image correlation for the high-speed deformation and fracture analysis of AISI 1045 and Ti6Al4V materials, Appl. Mech. (4) (2022) 3, https://doi.org/10.3390/applmech3040068.
[15] J.P.C. Bertoldo, E. Decencière, D. Ryckelynck, H. Proudhon, A modular U-Net for automated segmentation of X-ray tomography images in composite materials, Front. Mater. 8 (2021), https://doi.org/10.3389/fmats.2021.761229.
[16] R. Helwing, D. Hülsbusch, F. Walther, Deep learning method for analysis and segmentation of fatigue damage in X-ray computed tomography data for fiber-reinforced polymers, Compos. Sci. Technol. 230 (2022), https://doi.org/10.1016/j.compscitech.2022.109781.
[17] L. Hong, P. Zhang, D. Liu, P. Gao, B. Zhan, Q. Yu, et al., Effective segmentation of short fibers in glass fiber reinforced concrete's X-ray images using deep learning

technology, Mater. Des. 210 (2021), https://doi.org/10.1016/j.matdes.2021.110024.
[18] O.D. Pedrayes, D.G. Lema, R. Usamentiaga, P. Venegas, D.F. García, Semantic segmentation for non-destructive testing with step-heating thermography for composite laminates, Measure 200 (2022), https://doi.org/10.1016/j.measurement.2022.111653.
[19] K. Zheng, H. Chen, C. Wu, X. Zhang, Z. Ying, Z. Wang, et al., An improved dataset augmentation approach for deep learning-based XCT images segmentation in layered composite fabric, Compos. Struct. 317 (2023), https://doi.org/10.1016/j.compstruct.2023.117052.
[20] L. Cheng, Z. Tong, S. Xie, M. Kersemans, IRT-GAN: a generative adversarial network with a multi-headed fusion strategy for automated defect detection in composites using infrared thermography, Compos. Struct. 290 (2022), https://doi.org/10.1016/j.compstruct.2022.115543.
[21] J.-I. Caballero, G. Cosarinsky, J. Camacho, E. Menasalvas, C. Gonzalo-Martin, F. Sket, A methodology to automatically segment 3D ultrasonic data using X-ray computed tomography and a Convolutional Neural Network, Appl. Sci. (10) (2023) 13, https://doi.org/10.3390/app13105933.
[22] K. Nefs, V. Menkovski, F.P. Bos, A. Suiker, T. Salet, Automated image segmentation of 3D printed fibrous composite micro-structures using a neural network, Construct. Build. Mater. 365 (2023), https://doi.org/10.1016/j.conbuildmat.2022.130099.
[23] Q. Fang, C. Ibarra-Castanedo, X. Maldague, Automatic defects segmentation and identification by deep learning algorithm with pulsed thermography: synthetic and experimental data, Big Data Cogn. Comput. (1) (2021) 5, https://doi.org/10.3390/bdcc5010009.
[24] A. Ijjeh, P. Kudela, Delamination identification using global convolution networks, in: P. Rizzo, A. Milazzo (Eds.), European Workshop on Structural Health Monitoring, Springer International Publishing, 2023, https://doi.org/10.1007/978-3-031-07322-9_53.
[25] S. Ullah, A.A. Ijjeh, P. Kudela, Deep learning approach for delamination identification using animation of Lamb waves, Eng. Appl. Artif. Intell. 117 (2023), https://doi.org/10.1016/j.engappai.2022.105520.
[26] A. Badran, D. Parkinson, D. Ushizima, D. Marshall, E. Maillet, Validation of deep learning segmentation of CT images of fiber-reinforced composites, J. Compos. Sci. (2) (2022) 6, https://doi.org/10.3390/jcs6020060.
[27] Y. Ouassi, S. Ardchi, M.Y. El Ghoumar, M. Azzouazi, A weakly reiterative patches-wise framework for CT liver and lesions segmentation, Int. J. Intell. Eng. Syst. (6) (2022) 15, https://doi.org/10.22266/ijies2022.1231.47.
[28] X. Feng, J. Yang, A.F. Laine, E.D. Angelini, Discriminative localization in CNNs for weakly-supervised segmentation of pulmonary nodules, Med. Image Comput. Comput. Assist. Interv 10435 (2017), https://doi.org/10.1007/978-3-319-66179-7_65.
[29] S. Syed, K.E. Anderssen, S.K. Stormo, M. Kranz, Weakly supervised semantic segmentation for MRI: exploring the advantages and disadvantages of class activation maps for biological image segmentation with soft boundaries, Sci. Rep. (1) (2023) 13, https://doi.org/10.1038/s41598-023-29665-y.
[30] R. Singh, R. Garg, N.S. Patel, M.W. Braun, Generative adversarial networks for synthetic defect generation in assembly and test manufacturing, in: 2020 31st Annual SEMI Advanced Semiconductor Manufacturing Conference, ASMC, Saratoga Springs, NY, USA, 2020, https://doi.org/10.1109/asmc49169.2020.9185242.
[31] Z. Zhao, B. Li, R. Dong, P. Zhao, A surface defect detection method based on positive samples, in: X. Geng, B.-H. Kang (Eds.), Trends in Artificial Intelligence, Springer International Publishing, 2018, https://doi.org/10.1007/978-3-319-97310-4_54.
[32] J.-Y. Zhu, T. Park, P. Isola, A.A. Efros, Unpaired image-to-image translation using cycle-consistent adversarial networks, arXiv (2017), https://doi.org/10.48550/arXiv.1703.10593.
[33] M. Kim, H. Jo, M. Ra, W.-Y. Kim, Weakly-supervised defect segmentation on periodic textures using CycleGAN, IEEE Access 8 (2020), https://doi.org/10.1109/access.2020.3024554.
[34] S. Niu, H. Lin, T. Niu, B. Li, X. Wang, DefectGAN: weakly-supervised defect detection using generative adversarial network, in: 2019 IEEE 15th International Conference on Automation Science and Engineering, (CASE), Vancouver, BC, Canada, 2019, https://doi.org/10.1109/coase.2019.8843204.
[35] D. Hülsbusch, R. Helwing, S. Mrzljak, F. Walther, Comparison of the damage evolution in glass fiber-reinforced polyurethane and epoxy in the HCF and VHCF regimes investigated by intermittent in situ X-ray computed tomography, IOP Conf. Ser. Mater. Sci. Eng. 1 (2020) 942, https://doi.org/10.1088/1757-899X/942/1/012036.
[36] D. Hülsbusch, Charakterisierung des temperaturabhängigen Ermüdungs- und Schädigungsverhaltens von glasfaserverstärktem Polyurethan und Epoxid im LCF-bis VHCF-Bereich, Springer Fachmedien, Wiesbaden, 2021, https://doi.org/10.1007/978-3-658-34643-0.
[37] S.C. Garcea, Y. Wang, P.J. Withers, X-ray computed tomography of polymer composites, Compos. Sci. Technol. 156 (2018), https://doi.org/10.1016/j.compscitech.2017.10.023.
[38] P.J. Schilling, B.R. Karedla, A.K. Tatiparthi, M.A. Verges, P.D. Herrington, X-ray computed microtomography of internal damage in fiber reinforced polymer matrix composites, Compos. Sci. Technol. (14) (2005) 65, https://doi.org/10.1016/j.compscitech.2005.05.014.
[39] D. Hülsbusch, S. Mrzljak, F. Walther, In situ computed tomography for the characterization of the fatigue damage development in glass fiber-reinforced polyurethane, Mater. Test. (9) (2019) 61, https://doi.org/10.3139/120.111389.
[40] F. Milletari, N. Navab, S.-A. Ahmadi, V-Net: fully convolutional neural networks for volumetric medical image segmentation, in: 2016 Fourth International Conference on 3D Vision (3DV), 2016, https://doi.org/10.1109/3dv.2016.79. Stanford, CA, USA.
[41] P. Isola, J.-Y. Zhu, T. Zhou, A.A. Efros, Image-to-image translation with conditional adversarial networks, arXiv (2016), https://doi.org/10.48550/arXiv.1611.07004.
[42] J. Johnson, A. Alahi, L. Fei-Fei, Perceptual losses for real-time style transfer and super-resolution, in: B. Leibe, J. Matas, N. Sebe, M. Welling (Eds.), Computer Vision, Springer International Publishing, 2016, https://doi.org/10.1007/978-3-319-46475-6_43.
[43] H. Wang, S. Gui, H. Yang, J. Liu, Z. Wang, GAN slimming: all-in-one GAN compression by A unified optimization framework, arXiv (2020), https://doi.org/10.48550/arXiv.2008.11062.
[44] C. Chu, A. Zhmoginov, M. Sandler, CycleGAN, a master of steganography, arXiv (2017), https://doi.org/10.48550/arXiv.1712.02950.